RESEARCH ARTICLE

Experimental characterization of the turbulent intake jet in an engine flow bench

Cooper Welch[1] · Lars Illmann[1] · Marius Schmidt[1] · Benjamin Böhm[1]

Abstract

The turbulent intake flow of an optically accessible internal combustion engine is modeled using an air flow bench to reduce the complexity in the number of variables inherent within engine flows. By removing the piston and introducing a new optically accessible housing and outlet channel, the flow bench design simulates engine flows in the region just downstream of the intake valves and offers the possibility to measure and calculate quantities that would be difficult or impossible to obtain in the unsteady environment of a dynamic engine. Velocity data obtained via high-speed particle image velocimetry of the flow bench in the symmetry and valve planes are compared with data from a base operating condition of the motored engine at an intake pressure of 0.95 bar and a speed of 800 rpm at $-270°\text{CA}$ (270 crank-angle-degrees before compression top dead center), beginning with stationary valves at the corresponding valve lift of $-270°\text{CA}$, then with moving valves. Analysis of the intake jet turbulence for increasing mass flow rates reveals a coherent flapping of the jet at a frequency of 752.5 Hz for only the 100% mass flow rate case. The vortex shedding frequency of the valve stem is estimated to being in the range of 634–799 Hz, indicating a possible link between the coherent jet flapping and the vortex shedding surviving the acceleration through the valve gap. Through comprehensive analysis, this study provides valuable validation data and insight into the intake flows of internal combustion engines.

1 Introduction

The internal combustion engine (ICE) is likely to remain an important player in future global transport systems due to the unparalleled energy storage of combustible fuels. Therefore, the increase of efficiency and decrease of emissions continues to be a critical topic in the development of future highly optimized ICEs. One influential aspect of the cyclical performance of ICEs is the intake flow, which is linked in the deterministic causal chain of the combustion process (Dreher et al. 2021; Welch et al. 2023a). In particular, the high-velocity flow issuing from the valve gap into the cylinder, referred to as the intake jet, has been a focus of research as it is integral in engine phenomena such as the formation of the tumble (Borée and Miles 2015) or the rapid evaporation of fuel injections in spray-guided configurations. The intake jet of ICEs presents a challenging case for study due

to the complex interaction of the flows with dynamic engine geometries, namely the valves and the piston. To reduce the complexity for the development of high-fidelity engine simulation models, engine-relevant flows have been studied using flow bench configurations, in which the engine geometry is altered to allow a steady flow through the intake valve gaps to an open-ended cylinder. Using such configurations, the intake flow at certain steady valve lift positions can be considered as a temporal snapshot of the intake flow of the real engine at the corresponding valve lifts. Furthermore, time-averaged velocity data can be directly compared with the phase-averaged data of engine flows to validate the test case.

Over the last decade, improvements in the fields of diagnostics and computational engineering have allowed for the accurate study of flow bench configurations in high time and spatial resolution as well as in the 2- and 3-dimensional (2-and 3-D) space. Freudenhammer et al. conducted magnetic resonance velocimetry (MRV) experiments with the Darmstadt engine geometry under steady conditions using water as the fluid at matching Reynolds numbers (Re) to the motored engine at 800 rpm with intake pressure of 0.95 bar and a valve lift of 9.21 mm (corresponding to $-270°\text{CA}$,

✉ Cooper Welch
  welch@rsm.tu-darmstadt.de

1   Technical University of Darmstadt, Department
    of Mechanical Engineering, Reactive Flows and Diagnostics,
    Otto-Berndt-Str. 3, 64287 Darmstadt, Germany

that is 270 crank-angle-degrees before compression top dead center) (Freudenhammer et al. 2014, 2015). The MRV measurements established a database of high-fidelity 3-D velocity data of the intake flow for simulation model validation. Subsequent research employed air flow bench configurations to measure the velocity with 3-D, three-component (3 D 3 C) (Chen and Sick 2017), 2-D, three-component (2D3C) (Falkenstein et al. 2015, 2017), and 2-D, two-component (2D2C) (Buhl et al. 2017; El-Adawy et al. 2017; Falkenstein et al. 2020; Hartmann et al. 2016; Haussmann et al. 2020; Hyun and Ohm 2021; Liu et al. 2019) particle tracking velocimetry or particle image velocimetry (PIV). The majority of the aforementioned investigations are accompanied by computational fluid dynamics (CFD) studies, which complement the low-speed and 2-D experimental data by providing insight into the 3-D space as well as in the intake port where experiments with realistic engine geometries are difficult to conduct.

While a number of simulation studies in the literature have examined the turbulence of the intake flows in engine-relevant configurations, as of yet, no high-speed 2-D experimental data are available to validate spatial flow for the analysis of turbulence in an ICE flow configuration. This work aims to fill this gap by employing high-speed PIV in an air flow bench to characterize the intake flow of the optically accessible research engine of TU Darmstadt under various operating conditions. The use of high-speed PIV over tens of thousands of consecutive flow fields allows not only the computation of phase-locked quantities such as the turbulent kinetic energy, but also time-resolved statistics relevant for the characterization of the turbulence of the intake flow. This work is presented as follows: first, the experimental methods are introduced to describe the engine test bench and the flow bench adaptation, as well as the PIV setup and data processing techniques. Then, the results are presented and discussed beginning with the validation of the flow bench operating conditions in the symmetry and valve planes, then with the results of the turbulent analyses including an investigation of coherent jet flapping and its plausible sources. Finally, conclusions are drawn and recommendations for future work are given.

2 Methods

2.1 Engine test bench

The engine test bench used in this study is a single-cylinder optically accessible research engine which has been designed to offer consistent boundary conditions over a wide range of operating parameters (Baum et al. 2014). The quartz glass liner of the spray-guided cylinder head and quartz glass flat piston (with Bowditch extension) grant optical access (Freudenhammer et al. 2015; Geschwindner et al. 2020; Welch et al. 2020). The cylinder head configuration used has a compression ratio of 8.7:1 and allows a maximum planar field of view (FOV) of 75 mm ×55 mm (width × height) plus an extra 8 mm due to the pent roof. Although the engine can be fired with port fuel injection or direct injection (DI) of fuel, the operating condition (OC) used in this study is representative of motored (unfired) engine operation at 800 rpm and an intake pressure of 0.95 bar. This OC "A" was selected since it is one of the most studied OCs of the Darmstadt engine and it matches the condition used in the MRV experiments. As the focus of this study is to examine the intake flow of this engine in a simplified flow bench configuration, the reader is directed to (Baum et al. 2014; Schmidt et al. 2021; Welch et al. 2020, 2023b) for more information on the motored engine test bench.

2.2 Flow bench

An air flow bench has been designed to simulate the intake flow in the region near the intake valves of the engine in a simplified configuration by removing complexities derived from the moving piston. To that end, the piston was removed and a separate optical housing with an outlet channel replaced the original mirror housing of the engine to allow constant, uninterrupted flow from the intake valves to the outlet. Figure 1 shows the unchanged intake manifold of the engine test bench coupled with the spray-guided cylinder head and the flow bench housing section. The new optical section and outlet channel were designed such that no backflow was measured (verified via outlet channel PIV). The channel has a flat quartz glass bottom (optical plate) allowing the same bottom illumination for optical measurements as the motored engine configuration. The in-cylinder geometry was also simplified by removing the spark plug and inserting a smooth plug as well as by replacing the DI injector with a smooth-surfaced dummy. The air flow bench of this study with a stationary valve lift of 9.21 mm has already been used for validation and comparison of highly resolved wall-modeled LES techniques and has been demonstrated as a useful test case (Haussmann et al. 2020).

While the air flow bench offers a simplified geometry and test case, it closely simulates the real intake flow of the motored engine and offers direct comparison of dry air velocities. Since high-speed PIV can be applied, an improvement is made over the MRV measurements of the water flow bench conducted in the past (Freudenhammer et al. 2014, 2015). Furthermore, the complexity of the test case can be increased from stationary valves with steady-state turbulent flows to moving valves with dynamic flows closer resembling the intake velocity of the motored engine. In this study, the intake flow of the flow bench with stationary valves at 9.21 mm valve lift as well as moving valves is investigated,

Fig. 1 Flow bench experimental setup. Boundary conditions obtained from valve plane measurements are provided in Table 1
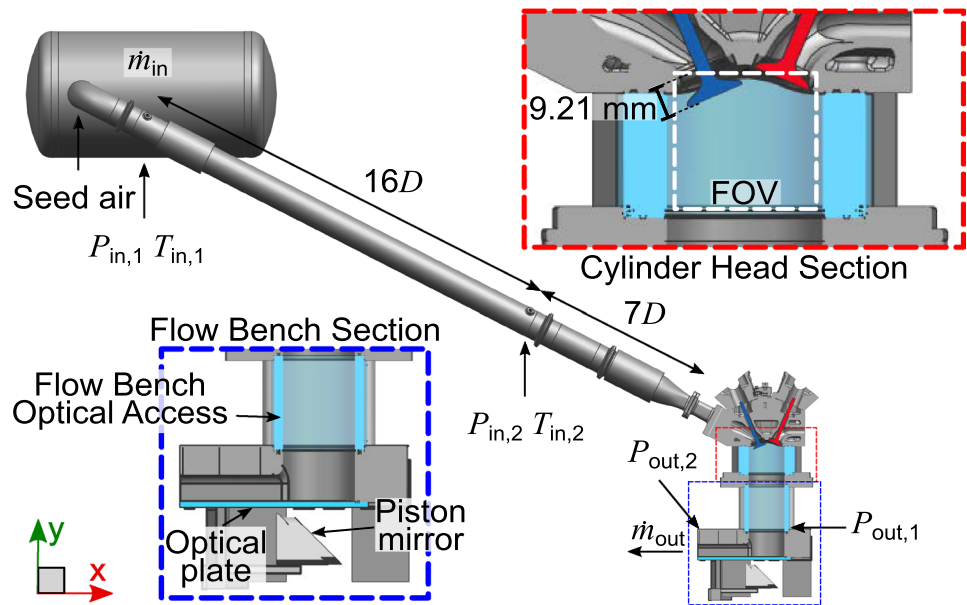
whereby the mass flow rates (MFRs) of the respective operating conditions (OCs) were set to match the intake velocity of the motored engine at $-270°$CA (see Sect. 3.1.1 for details on MFR selection). In addition, two more OCs at 75% and 50% MFR of the stationary (fixed) valve MFR were studied to include variations in Re. Table 1 shows the OCs of this paper with boundary conditions and estimated Re. The Re in Table 1 is calculated using the corresponding MFRs, the intake pipe diameter D of 56.3 mm as the characteristic length, and a dynamic viscosity μ of 1.83×10^{-5} kg/ms. The dynamic viscosity was obtained using Sutherland's law (White 2006). As displayed in Fig. 1, several pressure and temperature ports are located from the intake manifold to the outlet channel to provide comparison for simulations; the most relevant variables are provided in Table 1.

Figure 2 displays the phase-averaged pressure at various locations labeled in Fig. 1. Figure 2a shows the phase-averaged intake pressure measured just downstream of the noise reduction plenum and just upstream of the intake valves of a single motored engine run encompassing 400 consecutive cycles at 800 rpm and 0.95 bar average intake pressure. Despite the presence of plenums meant to reduce pressure oscillations, the regular movement of the valves

in combination with the long intake pipe characteristic of the research engine setup induces a coherent resonance in the pressure curves which must be considered when modeling the engine (Baum et al. 2014; Welch et al. 2020). Vertical dashed lines indicate the timing for the intake valve opening (IVO) and closing (IVC). Figure 2b displays the average intake pressure and the pressure at the end of the outlet channel for a flow bench experimental run with moving valves. Similar to the motored engine OC, the moving valves OC exhibits a coherent resonance due to the periodic intake flow. As soon as the intake valves close, the pressure in the intake manifold oscillates predictably; however, while the intake valves are open from 325°CA until -125 °CA, the amplitudes of the oscillations and the mean pressure decrease as the air flows into the open-ended cylinder. As shown in previous work by the authors, in the case of the motored engine, pressure oscillations during intake can have an effect on the velocity field; however, the influence on the velocity was larger when high-frequency oscillations induced by a backflow occurred (Welch et al. 2020). These backflows occur mainly in the part-load conditions when the higher in-cylinder pressure equalizes with the lower intake manifold pressure. Due to a lack of backflow in the flow

Table 1 Experimental boundary conditions. Standard uncertainties are indicated in parentheses

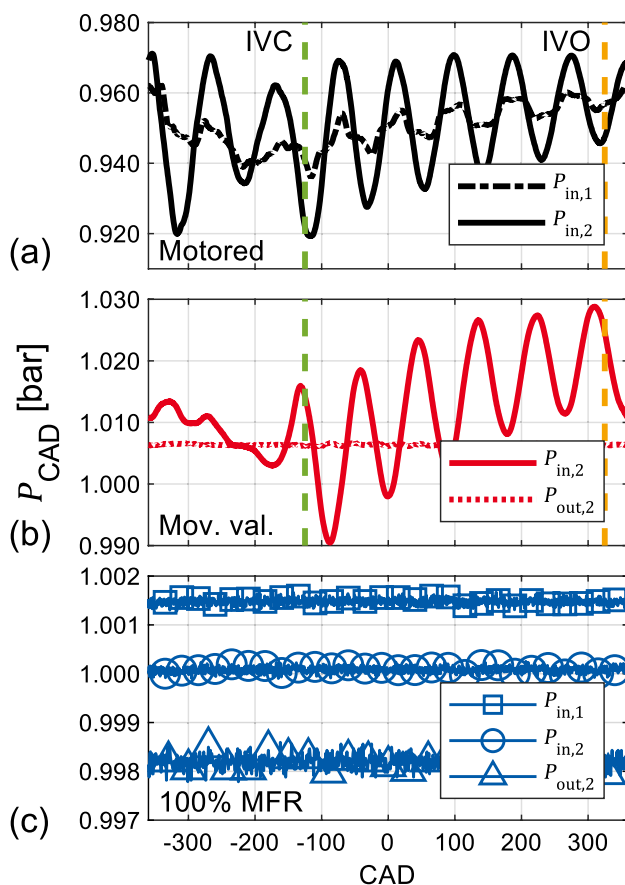| Condition	$\dot{m}_{in}$[kg/h]	$T_{in,2}$[°C]	$P_{in,2}$[bar]	ρ[kg/m^3]	Re [$-$]
Motored ($-270°$CA)	11.35(1.00)	35.7(0.5)	0.951(0.001)	1.07(0.001)	37200(est.)
Mov. val. ($-270°$CA)	19.90(1.00)	25.5(0.5)	1.011(0.001)	1.18(0.001)	–
100% MFR	94.10(1.00)	22.7(0.5)	1.000(0.001)	1.18(0.001)	32400(400)
75% MFR	70.63(1.00)	23.2(0.5)	1.006(0.001)	1.18(0.001)	24300(400)
50% MFR	47.09(1.00)	23.2(0.5)	1.004(0.001)	1.18(0.001)	16200(400)

Fig. 2 Phase-averaged pressure for motored engine (**a**), moving valve flow bench (**b**), and steady flow bench (**c**) operation. Intake valve opening (IVO) and closing (IVC) are indicated by the vertical dashed lines

bench (backflow also largely does not occur in the full-load motored case of this study), these influential high-frequency pressure oscillations do not occur and there is no observable effect on the flow, namely a spike in the intake flow (compare Fig. 5 of this work to Fig. 9 of (Welch et al. 2020)). Figure 2c displays the mean intake and outflow pressure of the steady flow bench at 100% MFR. Since this OC is a steady flow, the pressures are only phase-averaged and displayed on a CA-basis on the same horizontal axis as the top 2 panels of the figure for visualization purposes. From further upstream to the outlet, the pressure drops on average by less than 0.4%, yet it is a measurable difference just within the measurement uncertainties based on the sensor accuracy. One final consideration with the open configuration of the flow bench test stand is the state of the weather at the time of the measurement because the atmospheric conditions determine the pressure and the temperature of the system (relative humidity is held constant at approximately 1.8% by a condenser upstream of the air compressors), namely the ambient pressure can have a measurable effect on the outlet

pressure. Due to this reason, a pressure drop from $P_{in,1}$ to $P_{out,2}$ is not always observed, for example, when the ambient pressure is too high. Therefore, it is recommended that the MFR be used as a boundary condition for simulations of this flow bench configuration, rather than the pressure drop.

2.3 Velocity measurements

Velocity measurements were taken in separate experimental campaigns: first with the motored engine configuration at 0.95 bar intake pressure and 800 rpm (Exp. I) as a benchmark for comparison with the flow bench and the flow bench experiment (Exp. II). Both campaigns included the symmetry and valve-center planes (SP and VP) in non-simultaneous measurements of planar high-speed PIV. The experimental setup of both PIV planes in Exp. I is outlined in Welch et al. (2020), and the PIV setup of Exp. II is provided in Haussmann et al. (2020); however, Table 2 provides a summary of the optical setup, vector calculation, and processing of both campaigns. Figure 3 likewise shows a diagram of the PIV system for the flow bench. In short summary, high-speed PIV was conducted using pulsed laser sheets of two cavities with various time separation dt between pulses. Nebulized silicone oil (Dow Corning, DOWSIL 510) droplets were introduced to the intake pipe just upstream of probe locations of $P_{in,1}$ and $T_{in,1}$ indicated in Fig. 1 and allowed to mix well with the rest of the bulk mass flow of air. Image pairs were captured by high-speed CMOS cameras (see Table 2) in double-frame mode. Finally, after each measurement day or movement of the laser sheet, a series of target images from a 058-5 dual-plane calibration target from LaVision was captured to allow for scaling and dewarping of images before processing (based on 3rd-order polynomial).

2.4 Data processing

Processing and calculation of vectors were carried out using the commercial software DaVis (LaVision). Table 2 provides the detailed settings of the processing for each experimental setup. The methodology for the PIV processing follows the same formula: first, masking of raw images was done to remove reflective components such as the intake valves. Next, image pre-processing was conducted to prepare raw image pairs for vector calculation. Then, a multi-pass cross-correlation algorithm of decreasing interrogation window size was employed to calculate vector fields. Finally, vector post-processing was used to remove spurious vectors.

Velocity measurement uncertainties for the 100% MFR flow bench case were quantified by a correlation statistics approach described by Wieneke (Wieneke 2015) and applied using DaVis. The time-averaged uncertainty of the velocity magnitude of instantaneous flow fields varies locally. In the jet center of the VP near the valve and

Table 2 Summary of optical setups and vector processing for Exp. I and Exp. II

	I		II	
	SP	VP	SP	VP
Experiment				
Laser	EdgeWave Nd:YAG		EdgeWave Nd:YVO$_4$	
Sheet thickness [mm]	0.620	0.540	0.850	
dt at -270 °CA [µs]	9.0	9.3	10, 12, 18 (100%, 75%, 50%)	8.0, 11, 17 (100%, 75%, 50%)
Camera	Photron SA-X 2	Phantom v 1610	Phantom v 2640	
Lens	Sigma $f = 105$ mm $f/11 + 20$ mm extension rings		Nikon $f = 85$ mm $f/1.4 + 35$ mm extension rings	
Acquisition [Hz]	960	960	12500(12000 for MV)	
Processing				
Software	DaVis 8.4.0		DaVis 10.0.5	
Pre-processing	Spatial sliding background subtraction-8 pixel		Time filter subtraction	
Multi-pass iteration	Passes 1&2: 64×64, 50% overlap; passes 3&4: 32×32, 75% overlap		Passes 1&2: 48×48, 50% overlap; passes 3&4: 24×24, 75% overlap	
Post-processing	Peak ratio criterion < 1.3; universal outlier detection 7×7			
Interrogation window size [mm]	2.02	2.41	1.54	1.45

Fig. 3 Particle image velocimetry setup for the flow bench
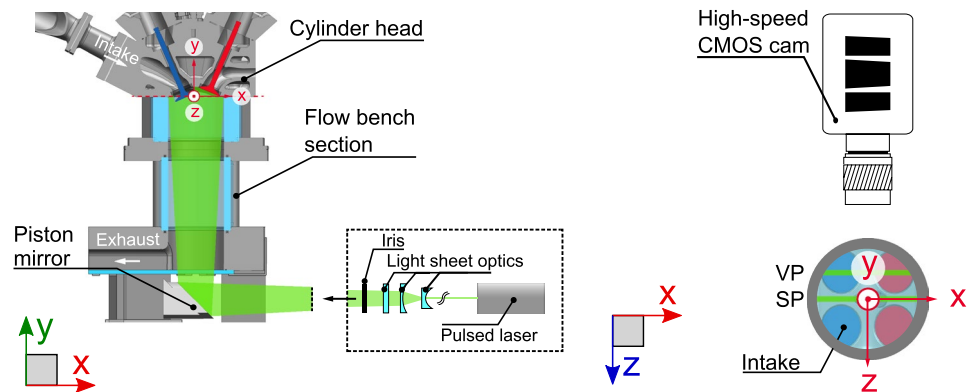
close to the cylinder wall, the uncertainty normalized to the maximum jet velocity is calculated to be approximately 4% and 10%, respectively. In the region below the center line of the intake jet where the highest velocity gradients occur, the normalized uncertainty is between approximately 6% and 9%. Further uncertainties that may not be accounted for in the approach from Wieneke, such as perspective errors, are discussed for the 100% MFR case by Haussmann et al. (Haussmann et al. 2020).

Measured pressure and temperature data were processed in MATLAB 2021 b for further analysis and visualization. Similarly, all further velocity data post-processing not shown in Table 2 and generation of figures were completed using MATLAB and some image post-processing (and creation of schematic figures) was conducted using Inkscape 1.2.

3 Results and discussion

3.1 Flow bench operating condition validation

In the following sections, the procedure for selecting the MFRs to properly simulate the intake flow of the motored engine at 800 rpm and 0.95 bar is outlined and a validation of the flow fields of the OCs is presented.

3.1.1 Selection of mass flow rates

The selection of the MFRs of the flow bench OCs was conducted by iteratively measuring the flow field in the SP and comparing the velocity field near the intake valves
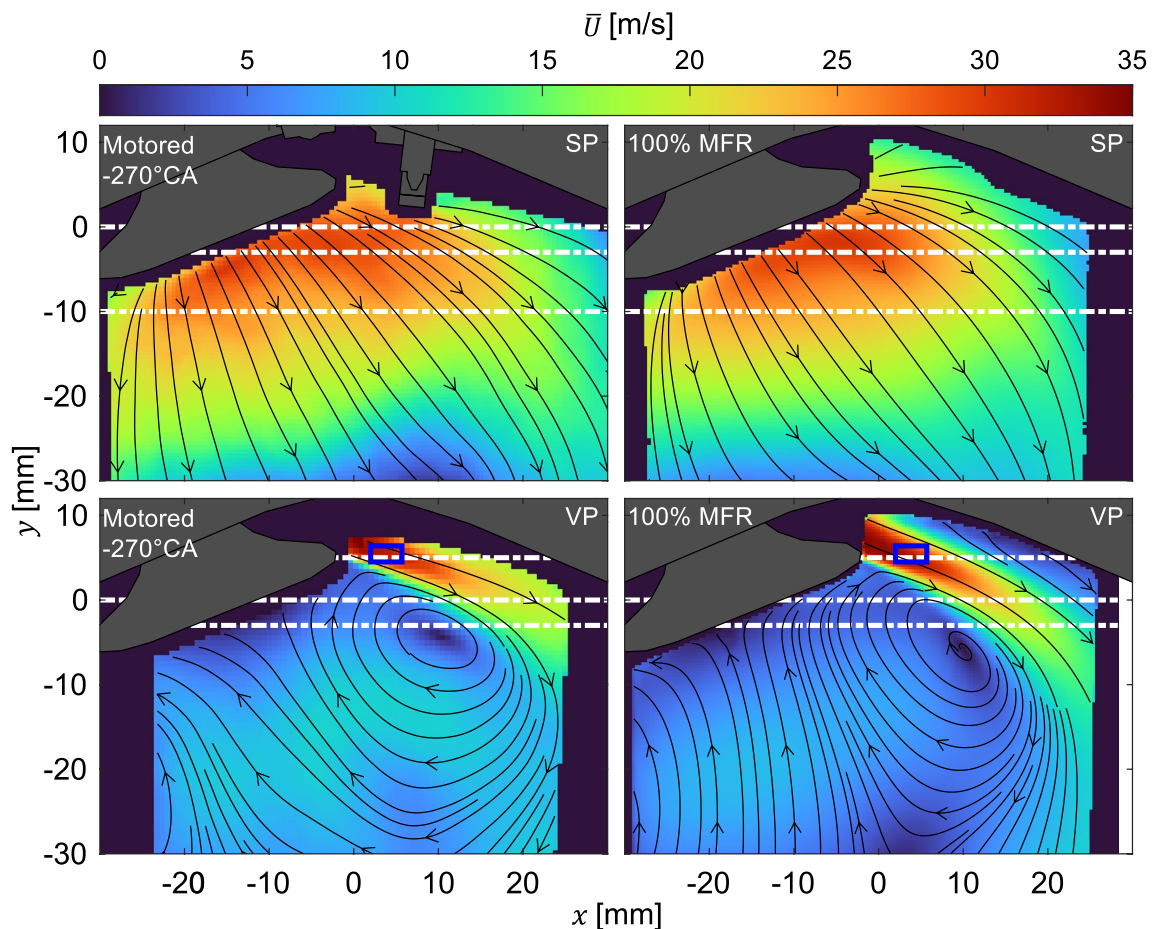
Fig. 4 Comparison of average velocity magnitude between the motored engine at −270°CA and the flow bench with 100% MFR. The mean velocity profile region of interest of Fig. 5 is represented by the blue box. Velocity profile lines for Figs. 6 and 7 are shown in white

to that of the motored engine at −270°CA. The upper section of Fig. 4 displays the mean flow field of the motored engine at −270°CA (left) and the fixed valve flow bench at 100% MFR (right) in the SP. White dot-dashed lines represent the y-axis locations for the velocity profiles of Fig. 6. Furthermore, the mean velocity magnitude and direction are shown by the color map and the streamline arrows, respectively. It can be observed that the number of resolved vectors in each FOV is different. This is due to changes in the experimental setup, for example, switching from VP to SP several times over the course of the experimental campaigns. Nevertheless, although the physical processes involved in motored engine intake are different than those of the stationary valve flow bench, namely the dynamic valve and piston motion facilitating the flow, the open-ended flow bench configuration still has the same mean intake flow structure in the SP directly downstream of the valves.

Using the stationary valve flow bench MFR obtained by examining the flow fields in the SP, the velocity fields in the VP are compared in the lower panel of Fig. 4. The white

dot-dashed lines represent the profile locations of Fig. 7. Also, in the VP, the mean intake velocity of the flow bench matches very well with the motored engine. Despite the smaller FOV of the motored case, the characteristic high-velocity intake jet with clearly defined shear and the formation of a tumble vortex appears in both configurations. In addition to the jets having similar trajectories, the velocity magnitudes along the jet match very well (compare Fig. 7 and Fig. 9).

The determination of the MFR for the dynamic valve flow bench configuration involved a similar iterative procedure as with the stationary valve case. However, with the moving valves OC, the mean intake jet in a region of interest (ROI) downstream of the intake valves (indicated by the blue boxes in Fig. 4) was used for the comparison of the velocity to the motored case, whereby the MFR was adjusted until the peak of the mean velocity profiles over time matched. Figure 5 shows the mean velocity profile comparison over CAD for the VP jet near the valve for the motored and moving valves flow bench cases at the selected MFR (Fig. 5a) and the valve lift and piston velocity over CAD (Fig. 5b). Although the
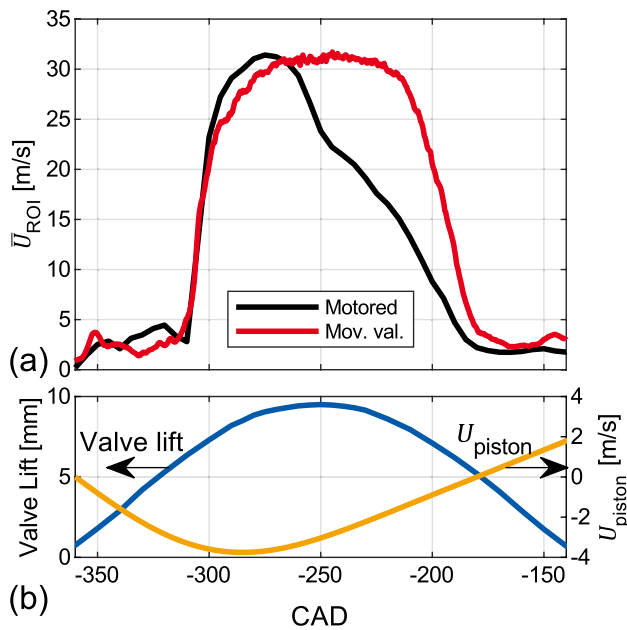
Fig. 5 a Mean intake velocity of the region of interest within the intake jet (blue boxes in Fig. 2) for motored and moving valves flow bench operation. **b** The intake valve lift curve (blue line, left axis) and the piston velocity (yellow line, right axis)

flow bench OC was designed to match the peak velocity of this profile to the motored engine, there is a slower, more symmetric decline of peak velocities. This is due to the fundamentally different flow process involved in the open-ended flow bench configuration. From the beginning of the IVO, a low velocity flow is present in the ROI for both cases; however, once the jet begins to form, the velocities of both OCs rapidly increase until they reach their maximum. In the case of the motored engine, as air enters the cylinder and the piston starts to decelerate, the intake velocity begins to decrease as the piston loses its sucking power and the flow meets resistance of the confined volume. This is not the case with the flow bench, however, as the in-cylinder air is allowed to pass through the outlet channel. Therefore, the resulting intake flow profile for the flow bench is symmetric and closely follows the intake valve lift curve. Despite contrasting intake velocity profiles over the whole intake phase, the velocity profiles of the intake jets are nearly identical before the piston reaches its peak downward velocity, resulting in similar velocities at the valve lift of interest, 9.21 mm.

3.1.2 Symmetry plane

As discussed in the previous section, MFRs were selected for the stationary valve flow bench case by comparing the velocity magnitudes in the SP to those of the motored engine operation. Figure 6 displays a profile comparison of the mean velocity x-and y-components $\bar{u}$ and $\bar{v}$, respectively,

as well as the mean velocity magnitude $\bar{U}$ at the three horizontal locations indicated in the upper section of Fig. 4. Since the MFRs of the flow bench were based especially on matching the velocity field of the motored engine in a region between $y = 0$ mm and $y = -3$ mm and $x = -10$ mm and $x = 10$ mm, all velocity components of the 100% MFR case compare well with the motored engine case. Additionally, the velocities of the lower MFR cases scale nearly perfectly with the reduction in MFR. However, there are characteristic differences between the flow bench and motored cases which merit closer inspection. First, although the sample size has no effect on the interpretation of the mean flow field (see Fig. 4), the smaller sample size is visible in increased fluctuations in the profiles, especially closer to the intake valves. While it is interesting to also examine the standard deviation of the profiles, especially when considering possible velocity fluctuations, standard deviation is discussed in detail in Sect. 3.2 Turbulence Analysis. A further difference between the velocity profiles of the 100% MFR case and the non-stationary valve cases is the slope and offset of the $\bar{u}$ profile starting at approximately $x > 0$ mm. This difference in velocity must be attributed to the motion of the valves since the moving valve flow bench case and motored case have nearly the same horizontal profile. The lack of the spark plug in all flow bench cases also rules out the influence of the spark plug on this increase in horizontal velocity present in both dynamic valve cases. Furthermore, due to the difference in horizontal velocity, the magnitude $\bar{U}$ is affected accordingly, despite very close profiles for the vertical component $\bar{v}$.

3.1.3 Valve plane

The valve plane velocity profiles, originating from the horizontal lines at the bottom of Fig. 4, are displayed in Fig. 7. As observed with the symmetry plane profiles in Fig. 6, the 100% MFR flow bench velocity profiles match well with the dynamic valve cases, especially closer to the valves; yet further away from the intake valves, the slopes for the dynamic cases change with the motored case displaying the least steep velocity slope. This indicates that the motored case has the intake jet with the furthest horizontal extension, an observation which may have been made by examining the flow field in Fig. 4. However, it may also be inferred from the profiles that the motored case has a slight shift in the jet's curl. This is not surprising since the intake velocity is constantly changing as the valves and the piston moves, resulting in a dynamic jet angle. Furthermore, the motored case generally has a weaker downward velocity component $\bar{v}$, despite having comparable $\bar{u}$ profiles to the other cases. This probably relates to the constantly changing jet curvature associated
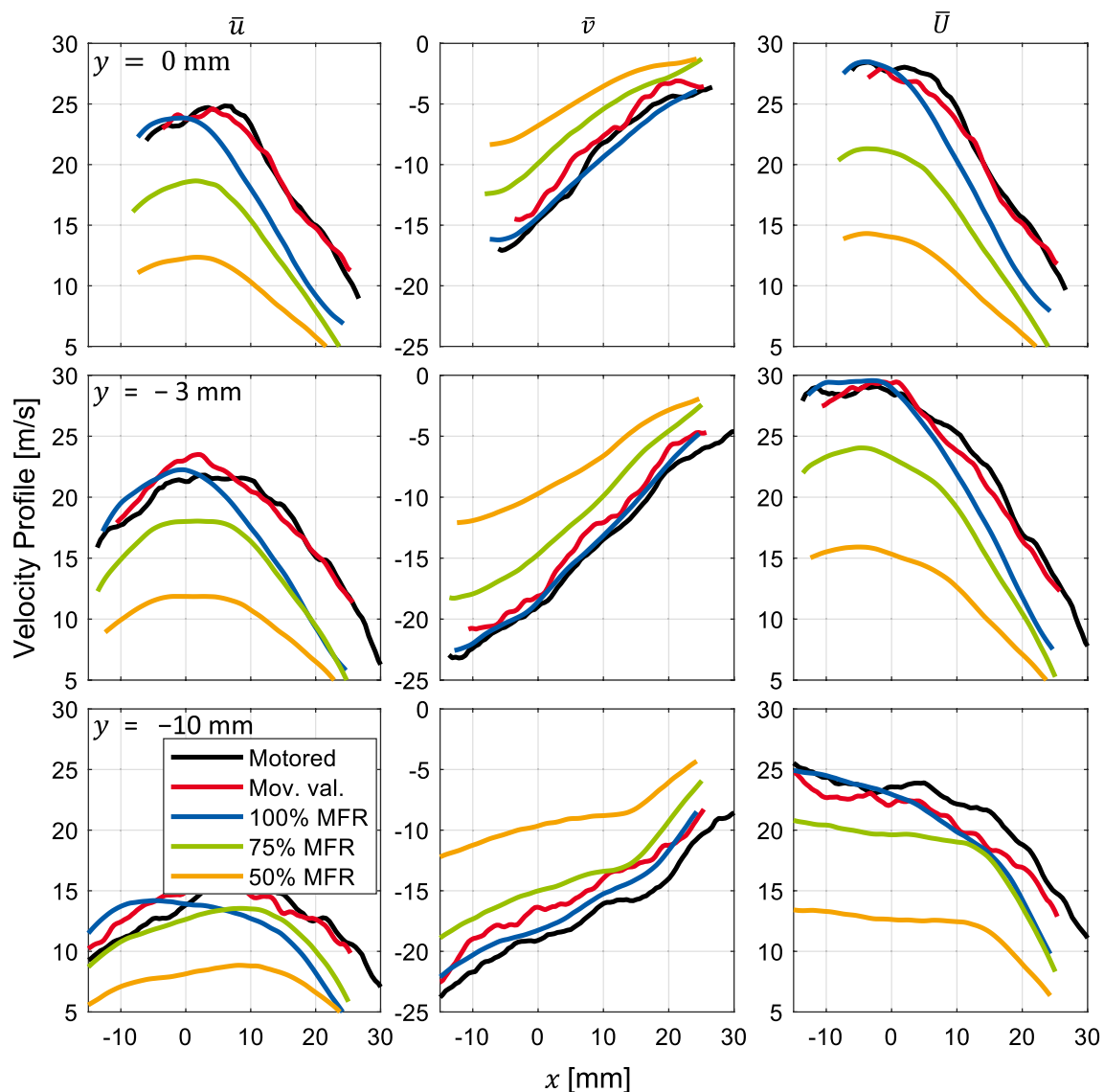
Fig. 6 Mean velocity profiles taken from the symmetry plane

with the combination of the moving valves and piston as well as the decreasing suction of the piston and more resistance due to the confined volume (compare Fig. 5).

To improve the comparability of the jets, a streamline of the mean intake jet is defined. Thereby, the centerline is defined by the 2-D streamline computed from a uniform starting position for all cases using the built-in MATLAB function *stream2* (The MathWorks, Inc. 2021). Figure 8a displays the defined jet profile and the newly defined streamwise component *s* and normal component *n* for the flow bench case of 100% MFR. First, the cartesian velocity components were interpolated along the streamline *S*.

Then, *s* and *n* were obtained by rotating the components by the local streamline angle θ_S:

$$\begin{bmatrix} \bar{s} \\ \bar{n} \end{bmatrix}_S = \begin{bmatrix} \cos\theta & -\sin\theta \\ \sin\theta & \cos\theta \end{bmatrix}_S \begin{bmatrix} \bar{u} \\ \bar{v} \end{bmatrix}_S \quad (1)$$

where the subscript *S* represents the position along the streamline. The origin point for the computation of the streamline was selected uniformly for all OCs such that the streamline intersects each jet through the center, beginning from the first position where a sufficient number of vectors are resolved to represent the center of the jet of the smallest FOV case; consequently, in the case of 100% MFR as
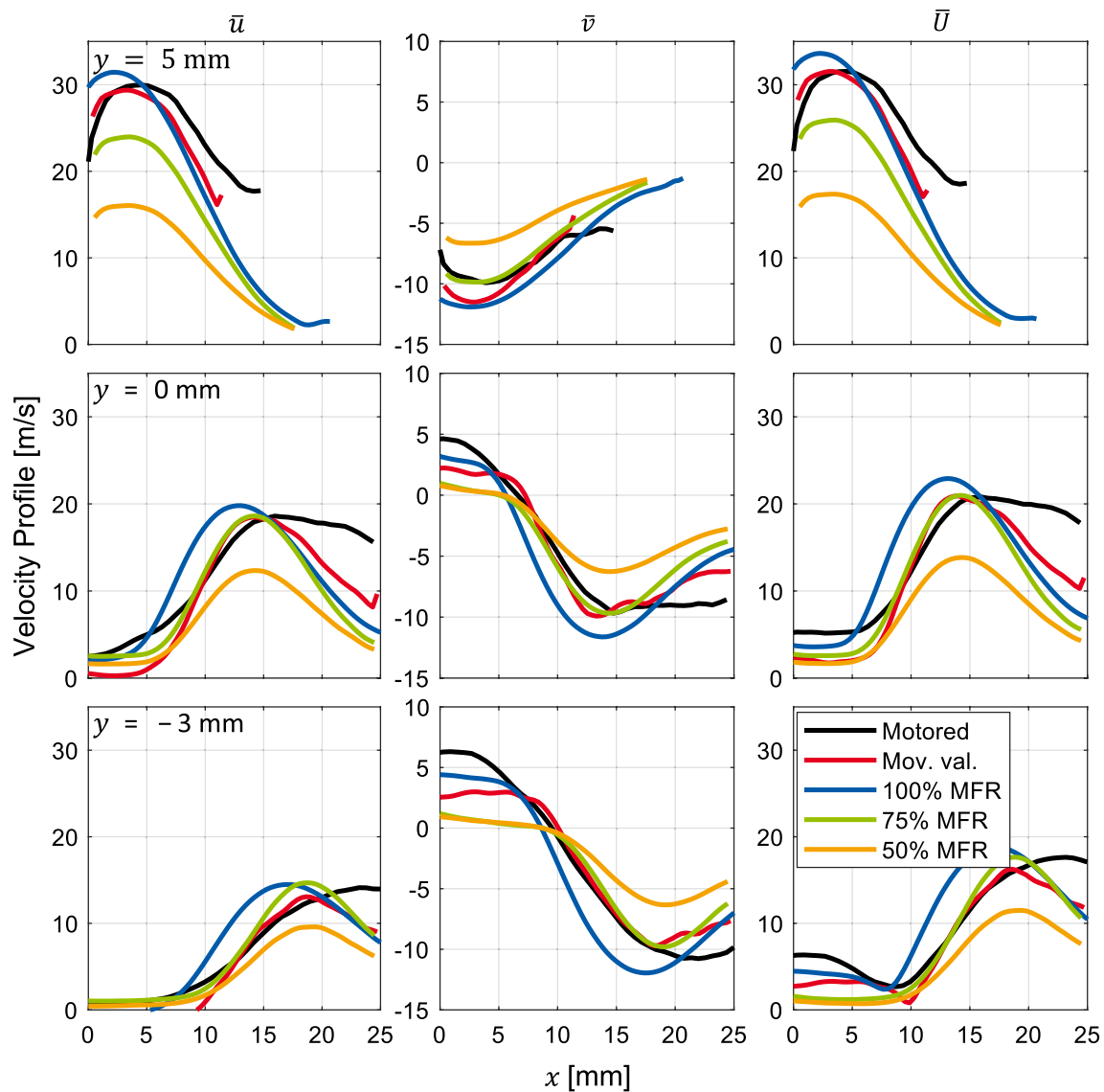
Fig. 7 Mean velocity profiles taken from the valve plane

shown in Fig. 8a, the origin is slightly downstream of the intake jet since Experiment II resolves a larger jet region than Experiment I. Figure 8b shows the different computed intake jet streamline trajectories. All cases have nearly identical trajectories in the first 15 mm along the streamline, with the exception of the motored case, which likely stems from differences caused by the presence of the piston and therefore the overall 3-D structure of the flow field. However, 15 mm downstream of the origin point, the trajectory of the 100% MFR case also begins to curl more heavily away from the cylinder wall and differs greatly from the other cases. Although it may be expected for such velocity profiles to differ further away from the origin, such a large discrepancy in the macroscopic flow structure of the main flow bench case merits further study (see Sect. 3.2 Turbulence Analysis).

The mean velocity profiles of components *s* and *n* along the streamline *S* are shown in Fig. 9. In Fig. 9a, the streamwise velocity along *S* for each case shows comparable values for the first 15 mm along *S*. It is interesting, however, that after a distance of 15 mm, the streamwise velocity of the 100% MFR case begins to sharply taper off and converge with the 75% MFR case, while that of the moving valves case decreases below the 75% MFR case. The decline of the slope of the mean streamwise velocity further from the valve exit corresponds well with a similar taper in the curl of the jet trajectory shown in Fig. 8b. As previously discussed, it is not surprising that after the initial strong shear region of the jet where the velocity gradient rapidly drops, which lasts until approximately 15 mm
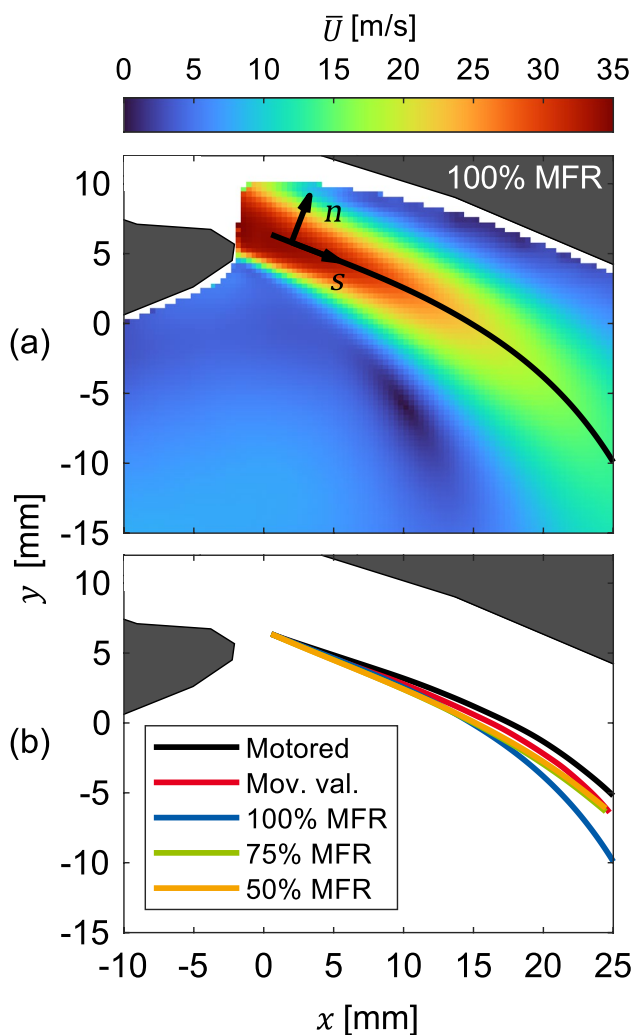
Fig. 8 **a** Example velocity magnitude in the valve plane and the streamline velocity components defined from a single origin in the middle of the intake jet for all cases. **b** Streamline trajectory for all cases
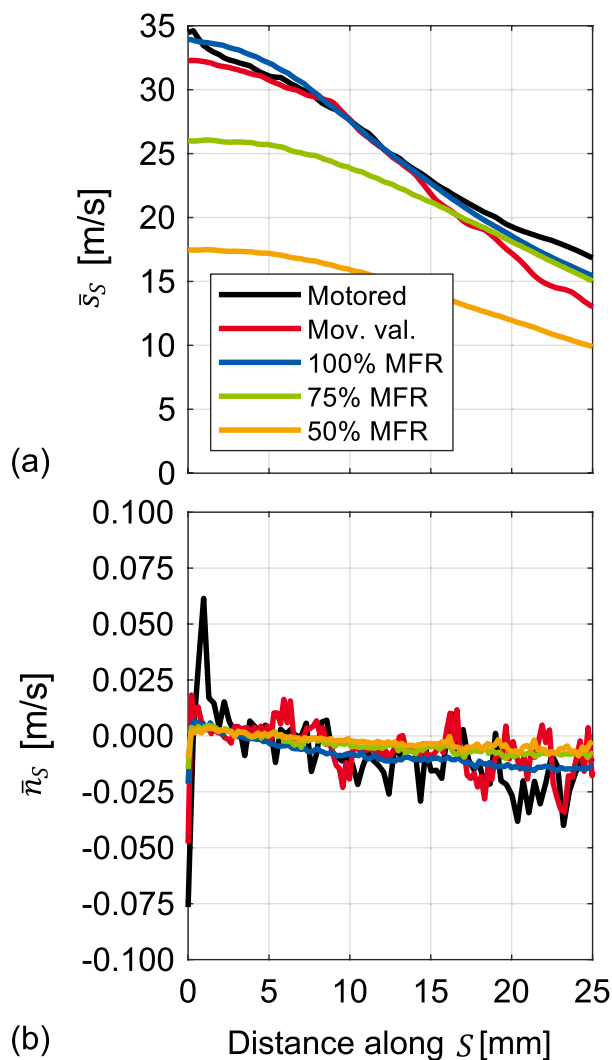

Fig. 9 **a** Mean velocity profile of the streamwise component s along the streamline. **b** Mean velocity profile of the streamwise-normal component n along the streamline

along S for the 100% MFR case (or 22 m/s for $\overline{U}$ from Fig. 8a), the mean streamwise velocities differ. However, it is noteworthy that the velocity profiles of the motored engine and moving valves cases exemplify stark contrasts from one another, demonstrating the impact of the moving piston and confined volume on the observed velocities. Additionally, Fig. 9b displays the mean normal component of velocity along the streamline. Per definition of a streamline, the mean normal component of velocity $\overline{n}_S$ is centered at a velocity of zero and consists only of the mean of the velocity fluctuations about the streamline. Therefore, the stationary valve flow bench cases, which each have a sample of 25000 consecutive flow fields, have the smoothest $\overline{n}_S$ curves. A further observation of Fig. 9b is the slightly

decreasing mean velocity along the streamline. Seeing as Fig. 9 only represents the mean streamline velocity components, the instantaneous fluctuations will be explored in the next section.

3.2 Turbulence analysis

Due to several dissimilar phenomena between the intake velocities in the SP and VP between each OC, such as the difference in slope of the velocity profiles for cases with similar Re at the exit of the valve, a detailed analysis of the turbulence is required to elucidate the causes for such contrasting results.

Fig. 10 Turbulent kinetic energy k for each operating condition. A multiplication factor is used to plot each condition with the same colorbar. White boxes in the top panels represent the region of interest for the calculation of $\overline{k}$ shown in Fig. 11
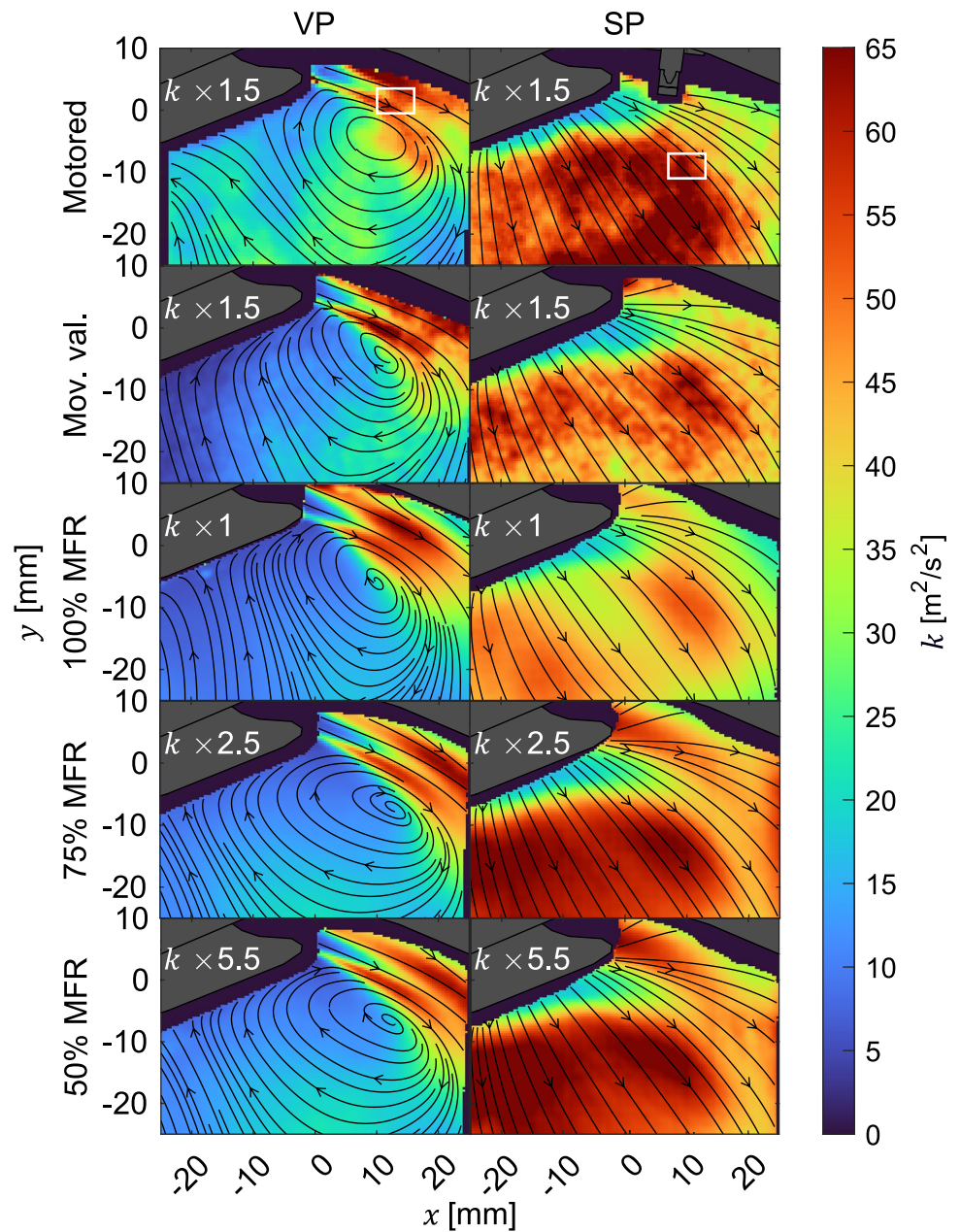
3.2.1 Turbulent kinetic energy

The turbulent kinetic energy k quantifies the amount of turbulence in a flow field through the difference in rms velocity fluctuations. For the purposes of this work which deals with 2-D planar velocity components, only the 2-D k is considered and can be defined as:

$$k = \frac{1}{2}\left(\left(\overline{(u')^2}\right) + \left(\overline{(v')^2}\right)\right) \qquad (2)$$

where the over-line bar represents the mean and the "prime" denotes the fluctuations from the mean. Turbulent kinetic energy therefore encompasses the standard deviation of the

velocity over both components. Figure 10 displays the k-field over all conditions and both measurement planes. For simpler visualization, each field shares the same color bar and contains a multiplication factor shown in the upper left corner of each panel. Additionally, mean flow directions are represented by the black streamline arrows and the white boxes shown in the motored panels represent the location for the ROIs of $\overline{k}$ displayed in Fig. 11. Despite the motored, moving valves, and 100% MFR cases each having similar mean velocities, the 100% MFR case clearly has the greatest number of fluctuations in the VP downstream of the jet's shear layer (region of the jet where the greatest velocity gradients occur, compare Fig. 4), indicated by the multiplication
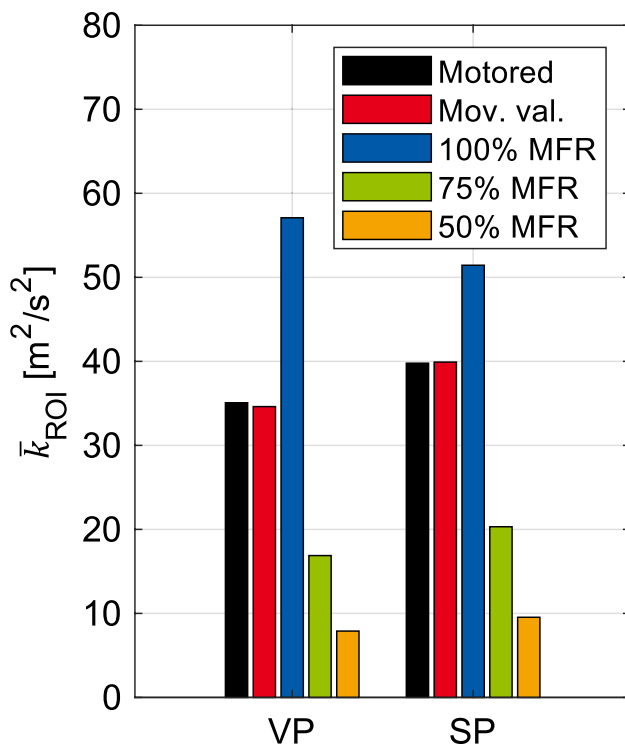
Fig. 11 Mean turbulent kinetic energy $\bar{k}$ in the white region of interest shown in Fig. 10

factor of only 1. Nevertheless, apart from the differences in required multiplication factor of k to share the color map, the shape of the fluctuations for each case is generally comparable. In each case, greater velocity fluctuations appear around the shear layer of the intake jet in the VP, meaning the highest velocity jet region is relatively stable and further away more variation occurs. Yet, the extent of this high k region in the 100% MFR case is slightly wider than the other stationary valve conditions, suggesting a wider flapping motion. Likewise, in the SP, the greatest k occurs downstream of the high-velocity region. However, the 100% MFR case in the SP exhibits a diagonal streak of comparatively lower k, while each other flow bench OC has a largely singular high-fluctuation region similar to the motored case. This observation indicates another characteristic of the 100% MFR case that differs from the others, meriting closer inspection of the OC (see subsequent section). Furthermore, a distinctive characteristic of the dynamic cases emerges: the fluctuations of the dynamic cases attenuate and disperse more quickly, while for the stationary valve cases the region of high fluctuations continues further toward the cylinder wall at +38 mm (VP case). This likely indicates further effects due to the dynamic movement of the valves, such as the presence of different vortices lingering from earlier CADs. In other words, the smooth k-field and jet velocity toward the wall of the stationary valve flow bench appears due to

the lack of dynamic effects since the jet continuously issues from the valve to the cylinder wall uninterrupted.

Rather than relying on the multiplication factors shown in Fig. 10, a bar graph comparison between the mean k within the white ROIs shown in Fig. 10 is displayed in Fig. 11. Assuming a constant turbulence intensity, k should scale quadratically with changes in mean velocity, for example, going from 50% MFR to 100% MFR, the velocity doubles; therefore, k should increase by a factor of four in the 100% MFR case. While this trend holds true for the dynamic valve conditions in comparison with the lower MFR cases, the 100% MFR case has more than 50% greater $\bar{k}$ in the VP than its dynamic counterparts. Subsequently, its ratios of 3.3 and 7.2 compared to the expected 1.78 and 4 of the 75% MFR and 50% MFR cases, respectively, are disproportionally high. This incongruity, especially in the VP, indicates there is likely more systematic flapping near the end of the jet than is present in the other conditions. Furthermore, since an abnormally great $\bar{k}$ appears for the 100% MFR case in both planes, which were measured on different days, it is not simply due to measurement error; rather, the OC itself possesses an abnormality which needs further investigation.

3.2.2 Coherent jet flapping

Further examination of the turbulence of the stationary valve flow bench operating conditions is required to interpret the contrasting observed k. Accordingly, the correlation R of the instantaneous streamline velocity components computed over all velocity fields at the fixed positions along S is calculated only in the fixed valve flow bench cases since they contain continuous data over the sample; in other words, successive velocity fields are correlated to one other. Figure 12a shows the mean autocorrelation of n at each position along S over all velocity fields, that is, the autocorrelation along the jet is calculated for each flow field sample, then the mean result over all fields is plotted. As observed with the analysis of k, the mean autocorrelation curve of the 100% MFR case has altogether different characteristics than the curves of the other two cases. While $\bar{R}_n$ of the 75% MFR and 50% MFR cases only crosses zero once and then continues to approach zero after a short peak, for the 100% MFR case, it crosses zero three times as the correlation peaks at least two more times after the first zero crossing. Seeing that the autocorrelation is calculated along the streamline, the presence of more than one peak after the first zero crossing indicates that there is potentially repeating structures in the jet due to the relatively high correlation value after the first zero crossing.

Figure 12b displays the autocorrelation curve of each stationary valve flow bench condition at the first position along S over all data points in the time series. Comparable to the mean autocorrelation curves of the normal component along S, the curves of the 75% MFR and 50% MFR cases
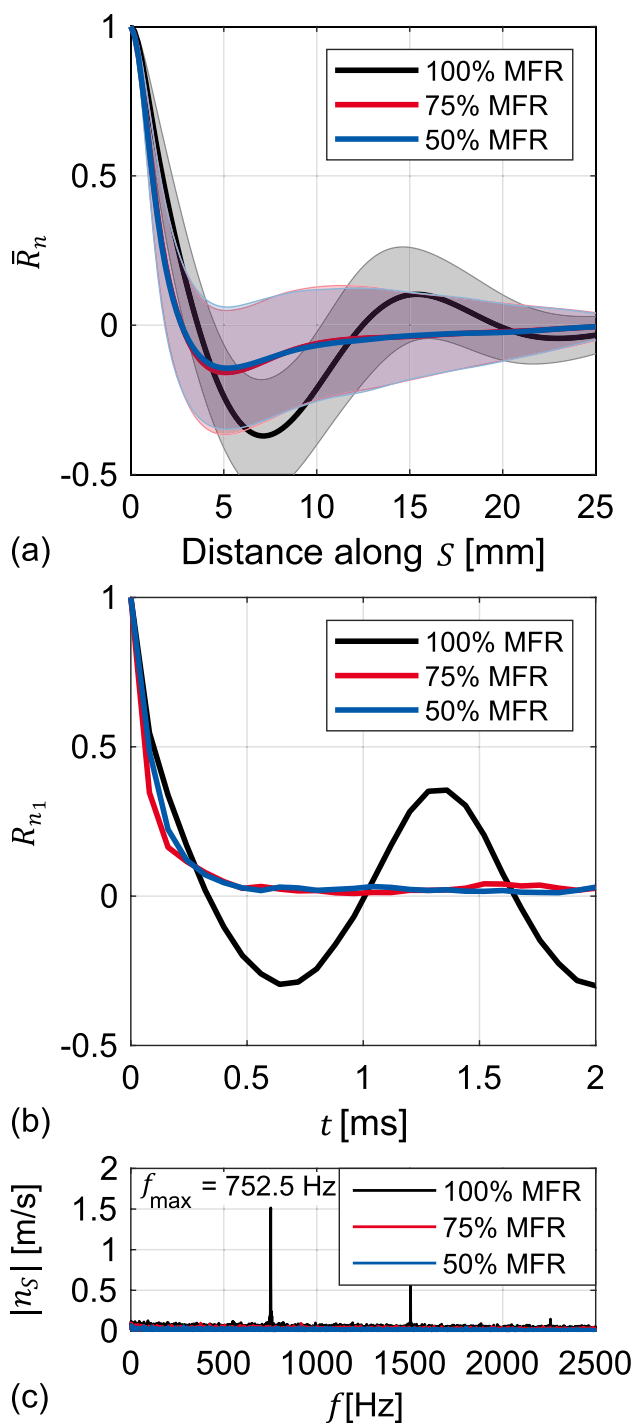
Fig. 12 **a** Mean (solid line) and standard deviation (shaded area) autocorrelation of n_S over all points in time. **b** Autocorrelation of n_S over the first position along the streamline. **c** Fast Fourier transform spectrum of n_S for the stationary valve flow bench

of Fig. 12b are different than that of the 100% MFR case. While the correlations of the lower MFR cases show exponential decay, the correlation of the 100% MFR case decays then crosses zero before following a continuous sinusoidal

pattern of peaks and valleys symmetric about zero. This process of repeating increasing and decreasing correlations over the time series indicates a repeating pattern in the flow. To further examine this observed pattern, Fig. 12c shows a fast Fourier transform (FFT) of the n component of velocity over the entire time series at the first position along S. The FFT reveals a dominant amplitude at a frequency of 752.5 Hz for the 100% MFR case with the second and third harmonic frequencies appearing with greater amplitudes than the surrounding frequencies. Since 752.5 Hz and its harmonic frequencies are the only positions on the FFT with high amplitudes and since the frequency range of dominant amplitudes is narrow, this indicates a highly repeatable flow pattern or flapping in the intake jet. Furthermore, Fig. 12c shows that the 75% MFR and 50% MFR cases do not have any dominant frequencies in the intake velocity at the first position along S and although it is not shown in this work, the FFT at all points along S yield the same result, pointing to purely stochastic jet flapping in these cases.

Due to the presence of a coherent jet flapping in the 100% MFR case, the structure of the jet and its flapping modes will be examined in the following. With a flapping frequency of 752.5 Hz and an imaging rate of 12.5 kHz, the flapping cycle repeats itself every 16.6 images. Over the entire sample of 25000 flow fields, the cycle is repeated 1506 times. In order to display the periodic flapping at four successive, evenly spaced phase angles of 0°, 90°, 180°, and 270°, mean interpolated flow fields have to be determined. Therefore, each 16.6 th flow field was computed by linear interpolation in time, for example, the 16.6 th image was computed from the 16 th and the 17 th instantaneous flow fields, and then the mean was computed at each phase. Here, phase refers to the cycle's relative position in time from index 1 to 16.6, for example, the first phase, phase 0, contains cycles 1, 17.6, 34.2, etc. Given the desired evenly spaced phase angles of 0°, 90°, 180°, and 270°, the corresponding instantaneous flow fields were again determined by an interpolation, and the averaged phases for the desired phase angles or index positions were determined (that is, index position 0, 4.15, 8.3, and 12.45, respectively). Then, a phase average was calculated. The resulting interpolated phases are displayed in Fig. 13. The right plot of each mode displays the computed centerline of the mean jet flow compared with that of the first mode at 0°. The mean flow fields in Fig. 13 show a progression of wave-like intake jets. Since the calculated phase averages show distinctly different flow fields with steep gradients close to the intake valves, the previously determined frequency of 752.5 Hz captures the behavior of the flapping well, indicative of a high stability of the amplitude and frequency. Furthermore, the overlapping centerline plots of the modes support this coherence through their corresponding links with the 0° mode, for example, the 180° mode has an inverted jet trajectory to that of 0°.

Fig. 13 Mean velocity field of the coherent jet flapping for the 100% MFR OP. The center line of flapping modes is compared with the phase at 0° (right side). Modes are obtained by calculating the mean of every 4.155 th field through interpolation
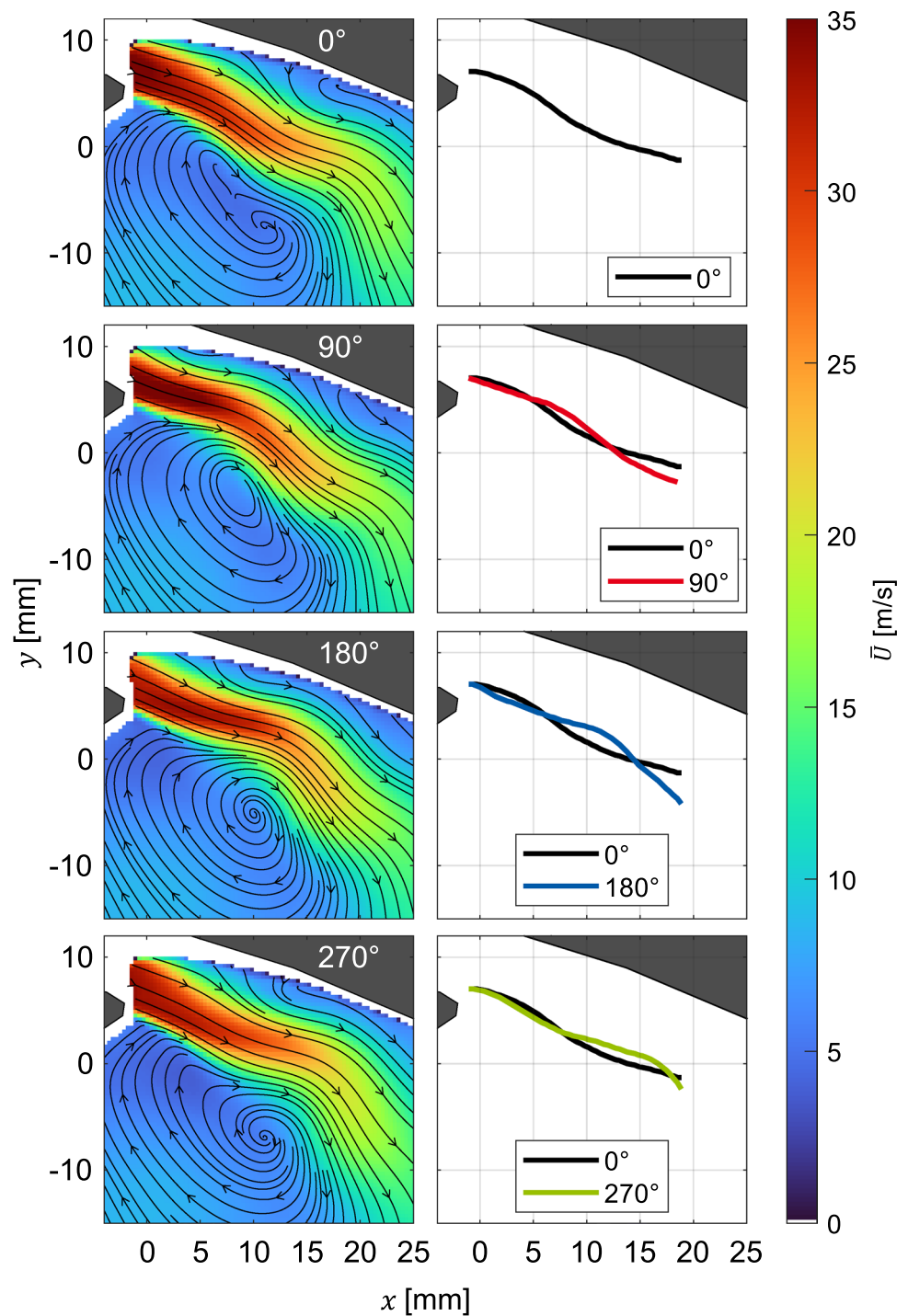
Although the flapping modes are well predicted, the origin of the coherent flapping with only the 100% MFR stationary valve case at 9.21 mm valve lift is less clear. A turbulent two-dimensional backward-facing step (BFS) flow offers a simplified problem in comparison to intake flows of IC engines, yet has complex fluid dynamic phenomena, such as the interaction between the reattaching shear layer and the recirculation zone, that precipitate unsteady flapping motion (Ma and Schröder 2017). The flow bench configuration is analogous to BFS flows in that a stream passes over a plane with a turbulent boundary layer (valve); then, a separated shear layer develops beyond the step (valve tip), and a recirculation zone forms below the shear layer. However, the flow bench intake flow must contend with more parameters, namely, the valve seat geometry which controls the acceleration of the flow through the valve gap and affects

the direction and shape of the intake jet (Freudenhammer et al. 2015), the cylinder roof which bounds the flow above the shear layer rather than below, the cylinder walls, which also direct the flow downward and augment the recirculation zone after impingement below the curved jet, and chiefly the vortex shedding at the valve stem of the highly turbulent flow. Cross-flow-induced vortex shedding has an immense impact on the stability of many engineering applications (Kaneko et al. 2008) and has been studied in the context of intake flows passing the valve stem of engines with steady flow bench configurations (Hartmann et al. 2016; Kapitza et al. 2010). A Karman vortex street forms in the wake of a cross-flow over a bluff body, in this case, the valve stem, when periodic vortex shedding occurs. The vortex shedding frequency f_w is expressed by the dimensionless frequency, the Strouhal number St, as:

$$f_w = \frac{\text{St}U}{D} \tag{3}$$

where St is a function of the Reynolds number Re, U is the stream velocity, and D is the characteristic length. The stream velocity was not obtained in the PIV experiments of this work since optical access in the intake ports is not possible in this configuration. However, the flow bench magnetic resonance velocimetry (MRV) measurements of Freudenhammer et al. (Freudenhammer et al. 2015) and the LES results of Haussmann et al. (Haussmann et al. 2020) under the same engine cylinder geometry, valve lift, and Re provide an estimate of the intake port velocity for the present operating condition of between 28 and 34 m/s. As in Hartmann et al. (Hartmann et al. 2016), the characteristic length D is taken as the hydraulic diameter, or 4 times the area divided by the wetted perimeter. As the valves are angled with respect to the intake flow, the wetted section of the valve stem is treated as an ellipse and the dimensions are calculated based on the angle of attack of the flow relative to the valve stem. With the angle of the free stream flow inside the intake pipe of 24° relative to the x-axis and the angle of the valve stem of 23° relative to the y-axis, the resulting angle of attack is 43°. The axes of the ellipse are therefore taken as the valve stem diameter of 7 mm and 10.3 mm $\left(\frac{7\text{mm}}{\sin(43°)}\right)$, and result in a hydraulic diameter of 8.3 mm. Based on the empirically obtained curve of Norberg (Norberg 2001) which plots St vs Re up to very high Re, St is likely within a range of 0.188 and 0.195 at Re between 15000 and 18200 based on the valve stem (ρ of 1.18 kg/m³, U of 28 m/s to 34 m/s, D of 8.3 mm, and μ of 1.83×10^{-5} kg/m s). Using the provided St and U ranges and the calculated D, the shedding frequency is estimated to being between 634 Hz and 799 Hz, which encompasses the observed frequency of 752.5 Hz. Although the exact values of St and U of this problem are not obtainable from the given

data, it is plausible that the vortices shedding from the intake valve stems are sustained through the acceleration of the valve gap leading to regular fluctuations of the intake jet in the 100% MFR case and not the others. Hartmann et al. (Hartmann et al. 2016) also demonstrated through their LES study of a similar flow bench setup that the velocity fluctuation frequencies at different locations downstream of the valve stem correspond approximately to the calculated shedding frequency, and they implied that the vortex shedding "survives" the acceleration through the valve gap having an effect on the jet. One key difference in the setup of the current study is that the observed flapping occurs in the measured $x - y$ plane, which is orthogonal to the vortex street ($x - z$) plane; nevertheless, velocity fluctuations in the vortex street plane can still have an effect on the measurement plane.

Although vortex shedding is a plausible source of the coherent jet flapping in the 100% MFR case, the other flow bench cases do not show evidence that such vortices persist through the valve gap. One possible explanation for this persistence through the valve gap in only the 100% MFR case is forced valve stem vibration induced by Karman vortex shedding. When considering a cylinder subjected to a cross-flow, synchronous vibrations are likely to occur when the shedding frequency approaches the cylinder's, or in this case, the valve stem's natural frequency (Kaneko et al. 2008). The valve stem alone likely has a natural frequency on the order of kHz since it is a rigid cylinder body; however, when in combination with the valve spring and the custom valve lift bridge, which is a pair of cylinders that compress and hold the valves and springs at 9.21 mm, a decrease in the system's natural frequency to the relevant shedding frequency range could be feasible. To assess this hypothesis, raw images of the intake valves were examined for signs of visible vibration. At a first glance, no movement of the valve in the measurement plane was visible in any of the stationary valve flow bench cases. However, the images were then examined at the laser reflection line where subtle movements were detected by changing image intensity I at pixels along the gradient of the peak I due to the laser reflection. Figure 14a shows a zoomed in example raw image of the valve and an exemplary point (in green, enlarged for visibility) along the laser reflection where I is sampled for an FFT. Figure 14b displays the resulting FFT of I at the extracted point from the second image of each PIV pair for the three stationary valve flow bench cases. The FFT reveals that once again in the case of only the 100% MFR case, there is a dominant frequency of 752.5 Hz. To rule out fluctuating laser intensity as a source of the dominant frequency of the FFT, the mean intensity of three distinct, equal-sized ROIs (indicated in Fig. 14a) is extracted and the resulting FFTs are displayed in Fig. 14c. The three ROIs were selected to display three different situations: ROI 1 is in the jet region
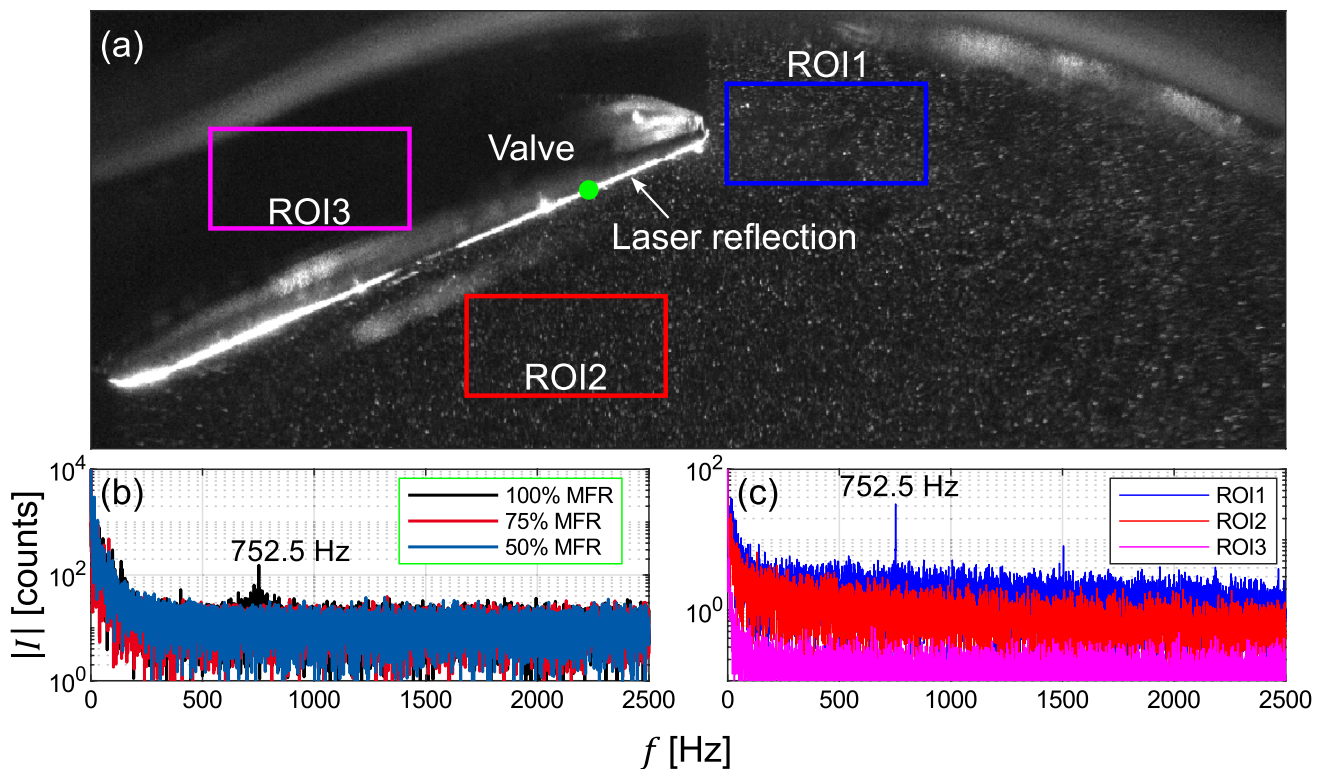
Fig. 14 a Zoomed-in snapshot of a PIV image showing the laser reflection along the intake valve. The green dot represents the location along the laser reflection where image intensity data are extracted for the FFT Fig. 14b. The three ROI boxes represent ROIs where the mean intensity is taken for the FFT in Fig. 14c. **b** Fast Fourier transform of the intensity at a point along the laser reflection on the bottom of the intake valve. **c** Fast Fourier transform of the mean intensity of different ROIs for the 100% MFR case

where particle voids are visible due to less Mie scattering where particles are unhomogenized due to the rotation of vortices. Here, despite the FFT using the mean I, which may smooth out the motion of the particle voids, the particle void structures coming in and out of the ROI have a clear effect on the FFT, showing the same frequency as the jet flapping and valve vibrations. Region of interest 2 is directly below the point extraction on the laser line and the mean I of this region has no dominant frequencies. Since ROI1 and ROI 2 have the same size window and similar mean I at a single snapshot, the laser itself does not have a significant fluctuation of intensity that creates artificial results in the FFTs. Finally, ROI 3 was selected to display a region of low signal where laser reflections are minimal and the particles are not illuminated to further rule out laser illumination fluctuations as the source for the detected frequency. The resulting FFT shows low signal without a laser reflection line or illuminated particles for contrast and no dominant frequency emerges. Therefore, since the particle void FFT of ROI 1 and the valve laser reflection point FFT show the same exact dominant frequency as the jet velocity, the observed jet flapping and the slight vibrations of the intake valves are related.

In previous work by the authors, it was demonstrated that intake pressure oscillations can have a large influence on the intake jet of the motored engine, which can switch the direction of the curl of the intake jet from up toward the cylinder roof to down toward the piston over the course of 10 CADs (Welch et al. 2020). The prescribed changes in the OCs of the flow bench experiment demonstrate that varying the flow condition within the intake pipe can have a great effect on the resulting flow, such as the presence of coherent flapping. Consequently, it is plausible that vortex shedding of the valve stem can have an effect on dynamic valves which would affect the development of the intake jet, and later, the tumble formation in the motored engine. Since vortex shedding occurs in the highly turbulent flows of the intake and since the intake of moving valves at different engine operating conditions offers a constantly changing environment, the critical flapping regime would likely occur only for specific and short time windows during the cycle. Furthermore, investigation of these phenomena in the motored engine is warranted in which a high spatial and ultra-high temporal resolution imaging system of the valve in combination with high-speed valve plane PIV would be employed to evaluate whether vibrations occur and if coherent flapping is detected within a cycle and if these phenomena have an effect on the flow in motored engine operation.

The presence of an unexpected coherent jet flapping in the 100% MFR case illustrates the need for accurate, full-scale numerical simulations in delineating different causes of cyclical variability in engines. In the case of the flow bench under 100% MFR conditions, the exact sources for the highly predictable jet flapping remain unknown. If in future studies it is found that there is a significant effect on motored engine flows due to measured coherent jet flapping, then simulations must employ larger domains to include the intake manifold as well as more sophisticated meshing tools to realistically capture phenomena related to the valve stem. Nevertheless, in spite of the coherent jet flapping that occurs only at the mass flow rate and valve lift (9.21 mm) of the 100% MFR operating condition of this study, the mean intake jet resembles that of the motored and moving valve flow bench cases. Therefore, the air flow bench of this work presents a challenging and realistic, yet simplified test case for numerical simulations. With the availability of data from configurations ranging from the simplified dynamics of stationary valve lifts of a single or different lifts (Haussmann et al. 2020) to more complex and realistic configurations such as the moving valves case presented in this work or the stationary valve flow bench with direct injection, the test cases offer a valuable opportunity to validate numerical models focusing on a wide range of engine applications from turbulence to wall models.

4 Summary and conclusions

This paper presents a detailed investigation of the development of an engine air flow bench based on the standard operating condition A (800 rpm at 0.95 bar) of the optically accessible single cylinder research engine at TU Darmstadt. The design of the flow bench allows a continual steady or dynamic (due to moving valve geometry) flow of dry air through the normal optically accessible spray-guided cylinder head combined with a smooth outlet channel with optical access. The MFR selection of the stationary and dynamic valve operating conditions was conducted to match the mean velocity field near the intake valves of the motored engine condition at $-270°CA$ (9.21 mm valve lift). The resulting mean flow fields show congruous velocity characteristics near the intake valve in the upper section of the field of view of the measurements. Mean horizontal line profiles of the velocity reveal slight deviations in the slopes of the flow bench profiles compared with that of the motored engine further away from the intake valves due to the lack of in-cylinder dynamics such as the motion of the piston and increasing resistance due to the confined volume shaping the direction and formation of a tumble vortex. However, the streamwise and normal velocity components to the streamline of the center of the intake

jet show even more agreement between the flow bench and motored conditions. Nevertheless, analysis of the turbulent kinetic energy revealed an unproportionate increase in velocity fluctuations present in the 100% MFR flow bench case. Through spatial and temporal autocorrelations of the flow fields along the streamline of the intake jet, it was also discovered that the 100% MFR flow bench case has a coherent flapping frequency of 752.5 Hz observable in the velocity fields. Using the observed dominant frequency, several velocity modes were reconstructed and resulting flow fields and jet trajectories show predictable flapping which is systematically repeated hundreds of times. An estimation of the vortex shedding frequency of the intake flow across the valve stem resulted in a possible range of between 634 Hz and 799 Hz, which indicates the vortices might survive the acceleration through the valve gap and they could have an effect on the flow. Furthermore, slight vibrations of the intake valve at the same flapping frequency were detected via changing intensity at pixels along the laser line reflection. The vibration was only detected in the flow bench case with the coherent flapping of the velocity field, which points toward a possible connection between the valve vibrations and the jet flapping. However, after extensive analysis, the causes of the coherent jet flapping in the 100% MFR remain unknown, which merits further investigation, especially with full-scale 3-D CFD simulations to delineate these sources.

The availability of flow bench data in various conditions with increasing complexity from stationary valves to moving valves or DI sprays with various MFRs provides the framework for the delineation of the intake flow's effects on engine phenomena and the development and validation of future CFD models. In future work, high-resolution intake valve imaging and simultaneous high-speed PIV of the intake jet in different motored engine conditions would be invaluable in determining whether significant valve vibrations or coherent jet flapping during engine operation occur and whether there is a subsequent effect on the flow characteristics leading up to ignition. Due to the presence of coherent jet flapping in the flow bench, researchers conducting high-fidelity 3-D simulations can choose to select conditions affected by such phenomena to test larger-scale domains, or they can avoid such conditions to accurately validate other modeling strategies such as the employment of new wall or spray breakup models.

Declarations

Conflict of interest The authors declare no competing interests.

Ethical approval This declaration is not applicable to this study.

References

Baum E, Peterson B, Böhm B, Dreizler A (2014) On the validation of LES applied to internal combustion engine flows: part 1: comprehensive experimental database. Flow Turbul Combust 92:269–297. https://doi.org/10.1007/s10494-013-9468-6

Borée J, Miles PC (2015) In-cylinder flow. In: Crolla D, Foster DE, Kobayashi T, Vaughan ND (eds) Encyclopedia of automotive engineering. Wiley, Chichester, pp 1–31

Buhl S, Hartmann F, Kaiser SA, Hasse C (2017) Investigation of an IC engine intake flow based on highly resolved LES and PIV. Oil Gas Sci Technol-Rev IFP Energies Nouv 72:15. https://doi.org/10.2516/ogst/2017012

Chen H, Sick V (2017) Three-dimensional three-component air flow visualization in a steady-state engine flow bench using a plenoptic camera. SAE Int J Engines 10:625–635. https://doi.org/10.4271/2017-01-0614

Dreher D, Schmidt M, Welch C, Ourza S, Zündorf S, Maucher J, Peters S, Dreizler A, Böhm B, Hanuschkin A (2021) Deep feature learning of in-cylinder flow fields to analyze cycle-to-cycle variations in an SI engine. Int J Engine Res 22:3263–3285. https://doi.org/10.1177/1468087420974148

El-Adawy M, Heikal MR, Aziz ARA, Siddiqui MI, Abdul Wahhab HA (2017) Experimental study on an IC engine in-cylinder flow using different steady-state flow benches. Alex Eng J 56:727–736. https://doi.org/10.1016/j.aej.2017.08.015

Falkenstein T, Kang S, Davidovic M, Bode M, Pitsch H, Kamatsuchi T, Nagao J, Arima T (2017) LES of internal combustion engine flows using cartesian overset grids. Oil Gas Sci Technol-Revue d'IFP Energies Nouv 72:36. https://doi.org/10.2516/ogst/2017026

Falkenstein T, Davidovic M, Chu H, Bode M, Kang S, Pitsch H, Murayama K, Taniguchi H (2020) Experiments and large-eddy simulation for a flowbench configuration of the darmstadt optical engine geometry. SAE Int J Engines. https://doi.org/10.4271/03-13-04-0032

Falkenstein T, Bode M, Kang S, Pitsch H, Arima T, Taniguchi H (2015) Large-eddy simulation study on unsteady effects in a statistically stationary SI engine port flow. In: SAE technical paper 2015–01–0373. https://doi.org/10.4271/2015-01-0373

Freudenhammer D, Baum E, Peterson B, Böhm B, Jung B, Grundmann S (2014) Volumetric intake flow measurements of an IC engine using magnetic resonance velocimetry. Exp Fluids 55:269. https://doi.org/10.1007/s00348-014-1724-6

Freudenhammer D, Peterson B, Ding C-P, Boehm B, Grundmann S (2015) The influence of cylinder head geometry variations on the volumetric intake flow captured by magnetic resonance velocimetry. SAE Int J Engines 8:1826–1836. https://doi.org/10.4271/2015-01-1697

Geschwindner C, Kranz P, Welch C, Schmidt M, Böhm B, Kaiser SA, De La Morena J (2020) Analysis of the interaction of spray G and in-cylinder flow in two optical engines for late gasoline direct injection. Int J Engine Res 21(1):169–184. https://doi.org/10.1177/1468087419881535

Hartmann F, Buhl S, Gleiss F, Barth P, Schild M, Kaiser SA, Hasse C (2016) Spatially resolved experimental and numerical investigation of the flow through the intake port of an internal combustion engine. Oil Gas Sci Technol-Rev IFP Energies Nouv 71:2. https://doi.org/10.2516/ogst/2015022

Haussmann M, Ries F, Jeppener-Haltenhoff JB, Li Y, Schmidt M, Welch C, Illmann L, Böhm B, Nirschl H, Krause MJ, Sadiki A (2020) Evaluation of a near-wall-modeled large eddy lattice boltzmann method for the analysis of complex flows relevant to IC engines. Computation 8:43. https://doi.org/10.3390/computation8020043

Hyun JH, Ohm IY (2021) TKE distribution according to the intake valve angle in steady flow of the pent-roof SI Engine. Int J Automot Technol 22:1003–1010. https://doi.org/10.1007/s12239-021-0090-7

Kaneko S, Nakamura T, Inada F, Kato M (2008) Flow-induced vibrations: classifications and lessons from practical experiences, 1st edn. Elsevier, Oxford

Kapitza L, Imberdis O, Bensler HP, Willand J, Thévenin D (2010) An experimental analysis of the turbulent structures generated by the intake port of a DISI-engine. Exp Fluids 48:265–280. https://doi.org/10.1007/s00348-009-0736-0

Liu D, Wang T, Jia M, Li W, Lu Z, Zhen X (2019) Investigation of the boundary layer flow under engine-like conditions using particle image velocimetry. J Eng Gas Turbines Power. https://doi.org/10.1115/1.4043444

Ma X, Schröder A (2017) Analysis of flapping motion of reattaching shear layer behind a two-dimensional backward-facing step. Phys Fluids 29:115104. https://doi.org/10.1063/1.4996622

Norberg C (2001) Flow around a circular cylinder: aspects of fluctuating lift. J Fluids Struct 15:459–469. https://doi.org/10.1006/jfls.2000.0367

Schmidt M, Ding C-P, Peterson B, Dreizler A, Böhm B (2021) Near-wall flame and flow measurements in an optically accessible SI engine. Flow Turbul Combust 106:597–611. https://doi.org/10.1007/s10494-020-00147-9

The MathWorks, Inc. (2021) MATLAB function reference: stream2. (2021st edn), Natick, MA

Welch C, Schmidt M, Illmann L, Dreizler A, Böhm B (2023a) The influence of flow on cycle-to-cycle variations in a spark-ignition engine: a parametric investigation of increasing exhaust gas recirculation levels. Flow Turbul Combust 110:185–208. https://doi.org/10.1007/s10494-022-00347-5

Welch C, Schmidt M, Geschwindner C, Wu S, Wooldridge MS, Böhm B (2023b) The influence of in-cylinder flows and bulk gas density on early spray G injection in an optical research engine. Int J Engine Res 24:82–98. https://doi.org/10.1177/14680874211042320

Welch C, Schmidt M, Keskinen K, Giannakopoulos G, Boulouchos K, Dreizler A, Boehm B (2020) The effects of intake pressure on in-cylinder gas velocities in an optically accessible single-cylinder research engine. In: SAE technical paper 2020–01–0792. https://doi.org/10.4271/2020-01-0792

White FM (2006) Viscous fluid flow, 3rd edn. McGraw-hill series in mechanical engineering. McGraw-Hill Higher Education, New York

Wieneke B (2015) PIV uncertainty quantification from correlation statistics. Meas Sci Technol 26:74002. https://doi.org/10.1088/0957-0233/26/7/074002